ACS Photonics

Letter

Cite This: ACS Photonics 2018, 5, 3485−3491

pubs.acs.org/journal/apchd5

Extraordinary Second Harmonic Generation in ReS_2 Atomic Crystals

Yu Song,[†] Siqi Hu,[†] Miao-Ling Lin,[‡] Xuetao Gan,*[,†] Ping-Heng Tan,[‡] and Jianlin Zhao*[,†]

[†]MOE Key Laboratory of Space Applied Physics and Chemistry, and Shaanxi Key Laboratory of Optical Information Technology, School of Science, Northwestern Polytechnical University, Xi'an 710072, China

[‡]State Key Laboratory of Superlattices and Microstructures, Institute of Semiconductors, Chinese Academy of Sciences, Beijing 100083, China

ABSTRACT: We report the observations of unexpected layer-dependent, strong, and anisotropic second harmonic generations (SHGs) in atomically thin ReS_2. Appreciable (negligible) SHGs are obtained from even (odd) numbers of ReS_2 layers, which is opposite to the layer-dependence of SHGs in group VI transition metal dichalcogenides, such as MoS_2 and WS_2. The results are analyzed from ReS_2's crystal structure, implying second harmonic polarizations generated from the interlayer coupling. Pumped by a telecom-band laser, SHG from the bilayer ReS_2 is almost 1 order of magnitude larger than that from the monolayer WS_2. The estimated second-order nonlinear susceptibility of 900 pm/V is remarkably high among those reported in two-dimensional materials. The laser polarization dependence of ReS_2's SHG is strongly anisotropic and indicates its distorted lattice structure with more unequal and nonzero second-order susceptibility elements.

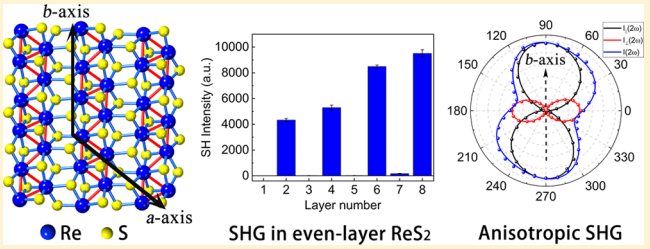

KEYWORDS: *second harmonic generation, transition metal dichalcogenides, rhenium disulfide, polarization, interlayer coupling, exciton resonance*

Atomically thin transition metal dichalcogenides (TMDCs) as one of the most important two-dimensional (2D) materials have drawn more and more attentions because of their intriguing physical and chemical properties resulting from structural symmetry and interlayer coupling.[1−3] High-performance 2D TMDC-based devices have been reported, including high-mobility field effect transistors,[4,5] ultrasensitive and broadband photodetectors,[6] low-threshold monolayer lasers,[7,8] and so on. Aside from the most popular TMDCs of group VI materials, for example, MoX_2 and WX_2, ReX_2 (X denotes Se or S) has recently attracted considerable interests due to their wholly unusual properties. First of all, unlike group VI TMDCs, ReX_2 grows in a distorted $CdCl_2$ structure and has strong anisotropy in the chemical bonds,[9−11] which consequently leads to the anisotropies of in-plane phonon, electrical, and optical properties.[12,13] For instance, Miao et al. reported the ratio of carrier mobilities along two principal axes of the few-layer ReS_2 exceeds 3. This crystallographic and concomitant electrical anisotropy were employed to construct good performance integrated digital inverters.[13] From a transient optical absorption measurement of a monolayer ReS_2, it is revealed the absorption coefficient and transient absorption are both anisotropic for light polarized parallel and perpendicular to the Re atomic chains.[14] The anisotropic Raman spectra[15,16] and linearly polarized excitons are revealed in few-layer ReX_2 as well.[17,18] Due to the intrinsically linear dichroism originated from the high in-plane anisotropy in few-layer $ReSe_2$, a polarization sensitive photodetection was implemented successfully.[19]

Second, the Peierls distortion in the 1T′ structure of ReX_2 prevents its ordered stacking and reduces the interlayer couplings, which have been demonstrated to be weaker than those in layered MoS_2.[16] In addition, few-layer ReX_2 behaves similar as monolayer ReX_2, including the direct bandgap, and slightly varied photoluminescence spectra with increased layer numbers.[20] This is in contrast to the group VI TMDCs, where crossover from indirect to direct bandgap occurs with decreasing the number of layers from bulk to monolayer. As a result, ReS_2-based photodetectors exhibit gate-tunable photoresponsivities competitive to those reported in photodetectors based on graphene, $MoSe_2$, GaS, and GaSe.[21]

Here, we reveal atomically thin ReS_2 has unique second harmonic generation (SHG), representing as the third distinct attribute from that in group VI TMDCs. It was reported that finite slices of group VI TMDCs with odd-layer thicknesses could yield moderately strong SHG due to the broken inversion symmetry. However, flakes with even numbers of layers are absent of SHG.[22,23] By examining SHGs in ReS_2 flakes with different layer-numbers, we find their SHGs exhibit an opposite dependence on the layer number, that is, even (odd) numbers of ReS_2 layers have strong (negligible) SHG. By analyzing the crystal structure, the layer-dependent inversion symmetry broken is revealed. In addition, we find the SH signal from a bilayer ReS_2 is about 1 order of magnitude stronger than that from a monolayer WS_2 when pumped by a telecom-band laser. A high second-order

Received: May 21, 2018
Published: August 10, 2018

DOI: 10.1021/acsphotonics.8b00685
ACS Photonics 2018, 5, 3485−3491

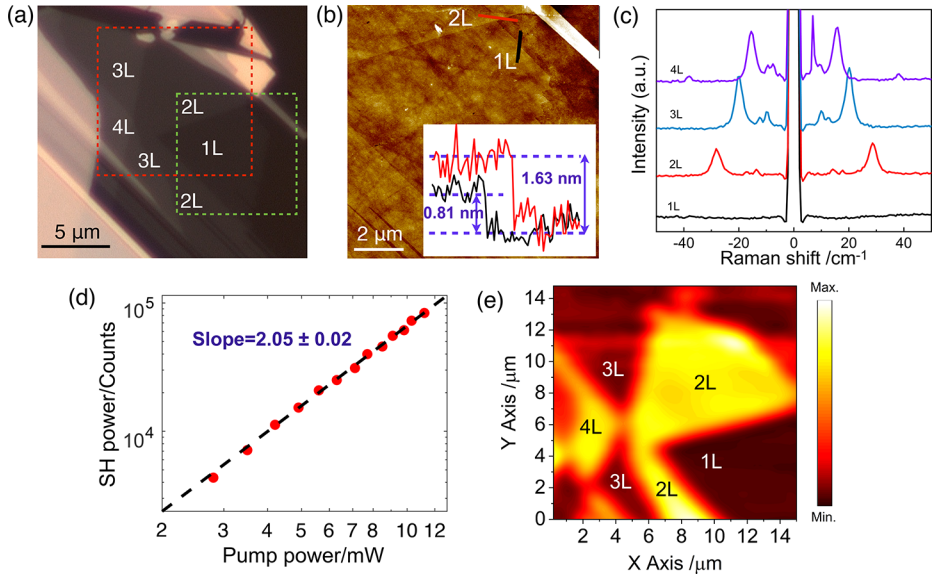

Figure 1. (a) Optical microscope image of the atomically thin ReS_2 sample exfoliated on a fused silica. (b) AFM image of the monolayer and bilayer ReS_2 crystals, which is indicated by the green dashed box in (a). The inset shows the thicknesses measured along the red and black solid lines. (c) Raman spectra from the ReS_2 flakes with different layer numbers. (d) Log vs log plot of the pump power dependence of SHG from the bilayer ReS_2. (e) SHG spatial mapping image of the ReS_2 area marked by the red dashed box in (a).

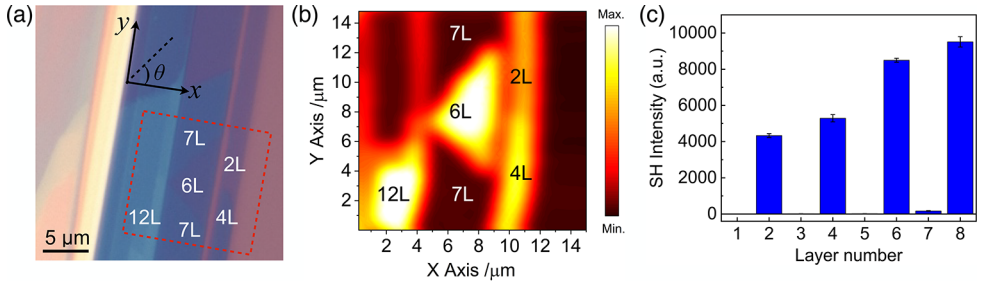

Figure 2. (a) Optical microscope image of a ReS_2 sample exfoliated on a silicon covered with 300 nm silicon oxide. (b) SHG spatial mapping image of the ReS_2 flake marked by the red dashed box in (a). (c) Experimentally measured layer dependence of ReS_2's SH intensities, where the uncertainties are indicated by the error bars.

nonlinear susceptibility in bilayer ReS_2 is evaluated exceeding 900 pm/V. The laser polarization dependences of the SHG in ReS_2 are discussed as well, showing a distinct anisotropy determined by the triclinic symmetry as well as a nonlinear susceptibility tensor with more nonzero elements. While the weak interlayer coupling in ReS_2 results in slight layer-dependences of Raman spectra, direct bandgap, and photoluminescence, our results unveil SHG in ReS_2 could strongly indicate the even or odd numbers of layers.

We implement the SHG measurements in a reflection geometry with a normal incidence excitation. A fiber-based pulsed laser is chosen as the fundamental pump radiation, which is centered around 1558 nm and has a repetition rate of 18.5 MHz and a pulse width of 8.8 ps. The pulsed laser is focused by an 50× objective lens with a numerical aperture of 0.75 into a spot size of about 2 μm on the sample. The SH signal scattered from the ReS_2 sample is collected by the same objective lens, which is then examined by a spectrometer mounted with a cooled silicon CCD. The reflected pump laser is filtered out from the SH signal by a dichroic mirror.

Atomically thin ReS_2 flakes are mechanically exfoliated on a fused silica or on a silicon covered with 300 nm silicon oxide. Figure 1a displays an optical microscope image of a sample with different numbers of layers on a fused silica, showing discernible regions with varied optical contrasts. The thick flakes are easy to break along a well-defined cleavage axis defined by the strong Re−Re atomic bond.[13,17] The layer numbers are evaluated by atomic force microscopy (AFM). Figure 1b shows the measured AFM image of a region marked by the green dashed box in Figure 1a. The inset shows the height data measured along the black and red solid lines with values of ∼0.81 and ∼1.63 nm, corresponding to the thicknesses of monolayer and bilayer ReS_2, respectively. Raman spectroscopy is a very accurate and efficient technique to distinguish layer numbers of 2D materials by measuring the ultralow-frequency rigid-layer shear modes, which is extremely sensitive to the interlayer coupling.[16,24,25] Figure 1c displays Raman spectra acquired from the different layers indicated in Figure 1a. In the Raman spectrum of the monolayer ReS_2, there is no ultralow-frequency Raman mode. The bilayer ReS_2 sample is confirmed from the emerging shear and layer-breathing modes at 13.8, 17.5, and 28.7 cm^{-1}. And the two shear modes at 13.8 and 17.5 cm^{-1} indicate the anisotropic stacking-order of the two ReS_2 monolayers.[16] The anisotropic trilayer and teralayer ReS_2 samples are recognized further by the numbers and peak positions of the rigid layer modes.[16]

In SHG measurements, we first focus the pump laser on the monolayer ReS_2 region, and no any SH signal is detected.

DOI: 10.1021/acsphotonics.8b00685
ACS Photonics 2018, 5, 3485−3491

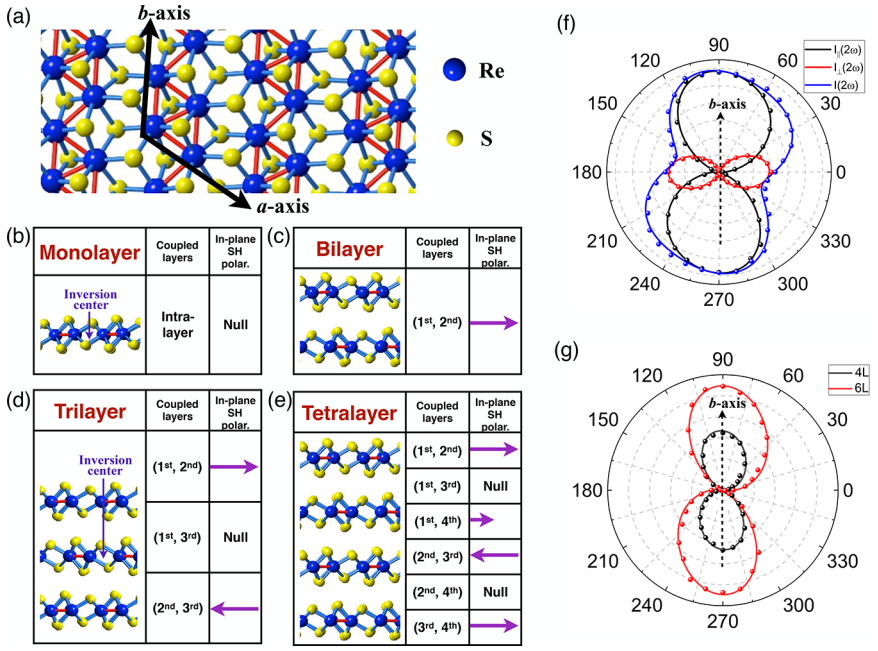

Figure 3. (a) Top view of the crystal structure of monolayer ReS_2. (b–e) Side views of crystal structures from mono- to tetralayer ReS_2. The model for explaining the relation between SH intensities and layer numbers is illustrated as well. In-plane SH polarization is assumed to be generated from the interlayer coupling. (f) Polar plots of the SH intensities from the six-layer ReS_2, showing SH radiation components detected parallelly and perpendicularly to the polarization of the pump laser as well as their summation. (g) Polar plots of parallel components of SH intensities from the tetralayer and six-layer ReS_2.

When the pump laser illuminates on the bilayer region, however, a strong frequency upconversion signal is obtained around the wavelength of 779 nm. To verify the SH character of the detected radiation, we measure its power dependence on the pump power, as shown in the log–log plot of Figure 1d. A nearly quadratic dependence on the pump power with a slope of 2.05 ± 0.02 is obtained, implying the second-order nonlinear process. Here, limited by the experiment system, the maximum pump power illuminated on the sample is about 11 mW. There is no observable saturation of the SH intensity at this power level. With even higher pump power, deviations from this second-order dependence are expected due to the material damage or electronic population pumping.[26,27] This result is totally different from those presented in group VI TMDCs, which has strong (zero) SHG in monolayer (bilayer) flake.[22,23] A SHG spatial mapping is then carried out over the ReS_2 region marked in the red dashed box in Figure 1a, including mono-, bi-, tri-, and tetra-layers. Figure 1e presents the SHG spatial mapping image, showing well-defined regions with varied SH intensities. Strong SH signals are observed over the bilayer and tetralayer regions, and the monolayer and trilayer flakes show zero or negligible SHG.

This layer-dependent SHG is confirmed further from another ReS_2 sample exfoliated on a silicon covered with 300 nm silicon oxide. The optical microscope image of the sample is displayed in Figure 2a. Examined by AFM, it has multiple thick layers, as noted in the optical microscope image. A SHG spatial mapping is implemented over the region marked by the red dashed box in Figure 2a, as shown in Figure 2b. The result agrees well with the conclusion revealed in Figure 1, showing strong (negligible) SH signals from the even (odd) numbers of ReS_2 layers. To conclude, we plot the layer dependences of ReS_2's SH intensities in Figure 2c, presenting sharp SHG contrast between even and odd numbers of layers. SHG in monolayer ReS_2 is absolutely zero, and SHG in other odd layers are no more than 0.5% of those in even layers. The high suppression of SHG in odd numbers of ReS_2 layers results from the existence of inversion symmetry, as expected from the bulk ReS_2 crystal. We also measure the SH signal from the bulk material and find it is negligible. Strong SHG in even numbers of ReS_2 layers indicate the broken inversion symmetry in their crystal structures.

To understand the absence (presence) of inversion symmetry in even (odd) numbers of ReS_2 layers, we draw the crystal structures from mono- to tetra-layer ReS_2 in Figure 3a–e. In monolayer ReS_2, each Re atom has six neighboring S sites and is sandwiched by the S atoms at both sides. Figure 3a shows the top view of a monolayer crystal structure. Different from group VI TMDCs, four adjacent Re atoms are bonded together to form a zigzag chain, presenting a distorted octahedral lattice structure. The rhombus formed by the four adjacent bonded Re atoms defines two principle axes, the *b* and *a* axes, which have an angle of 118.97°. The strong Re chain oriented along the direction of lattice vector *b*-axis endows ReS_2's strong anisotropies along the two principle axes, which also reduces its crystal symmetry to the lowest one among the TMDCs. When multiple ReS_2 monolayers stack into multilayer ReS_2 crystals, there are a variety of possible stacking orders. As demonstrated in ref 16, the most stable stacking configuration is that Re–Re bonds in the adjacent layers have an oriented angle of 60°, which forms an anisotropic-like multilayer ReS_2. Figure 3b–e displays the side views of the crystal structures from mono- to tetra-layer ReS_2. In monolayer ReS_2, there is only one symmetry operation, that is, the inversion symmetry *i*. The inversion center is indicated by the arrow. The same symmetry operation holds for other odd numbers of layers, as well as a bulk crystal. ReS_2 crystals with this low crystal symmetry belong to the C_i space group. In even numbers of ReS_2 layers, the symmetry operation is reduced further with the broken inversion symmetry, as illustrated in the bilayer and

DOI: 10.1021/acsphotonics.8b00685
ACS Photonics 2018, 5, 3485–3491

tetralayer crystal structures. Therefore, the even numbers of layers belong to the noncentrosymmetric C_1 space group.

In Figure 3b−e, combining with the transformations of crystal symmetry for different layer numbers, we also illustrate a simple model to analyze the layer-dependent SH intensities. The inversion symmetry in monolayer ReS_2 makes its SHG to be exactly zero. In bilayer ReS_2, each layer can not generate SH signal either due to the intralayer inversion symmetry. Hence, the observed strong SH radiation in bilayer ReS_2 could be attributed to the appreciable SH polarization generated from the interlayer coupling. It is consistent with the inversion symmetry broken when the two monolayers stack into a crystal structure shown in Figure 3c. The crystal structure also indicates that the interlayer SH polarization should result from both the in-plane and out-of-plane dipoles. Considering the low numerical aperture of the employed objective lens, our experimentally measured SH signal mainly arises from the in-plane SH polarization. We therefore use the in-plane SH polarization to qualitatively explain the layer-dependent SHG, as shown in Figure 3b−e. By using a tilted far-field microscopy,[28] near-field plasmonic modes,[29,30] or manifold field-gradients in a surface-plasmon,[31] the out-of-plane SH polarizations could be further examined in future work. With the measured in-plane and out-of-plane SH polarizations, a complete model of SH polarizations induced by the interlayer coupling could be constructed.

We assume the bilayer structure generates an in-plane SH polarization orientating to right. In the trilayer ReS_2 shown in Figure 3d, the coupling between the first and second layers should yield an in-plane SH polarization orientating to right as well. However, the in-plane SH polarization due to the coupling between the second and third layers has a reversed direction. The cancellation of the two SH polarizations results in the undetectable SH radiation. In addition, the first and third layers may couple with each other as well. However, they are symmetrical around the inversion center indicated by the arrow in Figure 3d, which therefore would not generate SH polarization. However, as indicated in Figure 2c, SHGs in other odd numbers of ReS_2 layers, such as five-layer and seven-layer, have nonzero values. It can be attributed to the small but finite optical phase shift between different SH polarizations generated by units of each adjacent layers,[23] which hinders their complete cancellations with respect to the inversion center.

The SH intensity from the tetralayer ReS_2 could be analyzed in the same model, as shown in Figure 2e. If we consider the SH polarizations generated by second-third layers coupling and third-fourth layers coupling cancel out each other, the coupling between the first and second layers would yield an extra SH polarization. In addition, if the interlayer coupling between the first and fourth layers were considered as well, there would be a SH polarization as well, which is smaller than that generated by the adjacent layers due to the weaker interlayer coupling. Thence, corresponding to the results shown in Figure 2c, SHG in tetralayer is higher than that in bilayer. For thicker even numbers of ReS_2 layers, SHG increases gradually because of more extra SH polarizations. This increment of SH intensities in different even numbers of ReS_2 layers is unique compared to the variations of SH intensities in group VI TMDCs or boron nitride, which have constant net SH polarizations in different odd numbers of layers.[23] The revealed SHG attribute also indicates while ReS_2 has the Peierls distortion, its interlayer coupling is strong enough to provide remarkable second-order nonlinearity.

Polarization-dependent SHG is a useful technique to investigate the crystal symmetry of 2D materials. We measure the polarization dependences of the SH signals from the even numbers of ReS_2 layers. In the measurements, the pump laser is converted into different linear polarizations by passing a circularly polarized laser through a rotated polarizer. Another polarizer is placed in the signal collection path, whose direction is rotated accordingly to detect SH radiation components parallel or perpendicular to the polarization of the pump laser. Figure 3f displays the polar plots of the parallel and perpendicular components of the SH intensities from the six-layer ReS_2 shown in Figure 2a. In Figure 2a, a coordinate is assigned, where the y axis is along the ReS_2's b axis and the x axis is perpendicular to the y axis. The polar angle θ is the one between the laser polarization direction and x axis. For the parallel and perpendicular components of the SH intensity, both of them show polarization dependences with shapes of dumbbell, which are consistent with the predictions from the low crystal symmetry in C_1 space group. In the parallel component, the dumbbell is twisted due to the distorted crystal structure. Also, when the polarization of the incident light is parallel to the b-axis, the SH signal is exactly maximum. For the perpendicular component, the polarization-dependence presents a dumbbell as well, while there is no observable distortion. The maximum SH intensity is obtained when the laser polarization is along the x-axis. Since the anisotropic properties, the maximum SH intensities of the parallel and perpendicular components have a ratio of ∼2, which yields an anisotropic distribution of the total SH intensity. This is different from that obtained from a group VI TMDC, which has an isotropic total SHG intensity.[23] We also measure the polarization dependences of SH intensities from samples with different layers, as shown in Figure 3g. The parallel components of SH intensities from the tetralayer and six-layer in Figure 2a present the same twisted dumbbell shape with different maxima, implying the same crystal orientation for the two flakes. These SHG's polarization dependences provide a straightforward optical method for determining the crystallographic orientation of 1T′ ReS_2.

The polarization dependent SH intensities could be analyzed from the second-order nonlinear susceptibility tensor $\mathbf{d}$. We describe the SH polarizations $\mathbf{P}$ from the matrix calculation of $\mathbf{P} = \mathbf{dE}$ in the x−y coordinate defined in Figure 2a. The pump laser is incident along the z axis. By expressing $\mathbf{P}$ and $\mathbf{E}$ into their components in x, y, and z directions, the matrix calculation is given by[32,33]

$$\begin{bmatrix} P_x(2\omega) \\ P_y(2\omega) \\ P_z(2\omega) \end{bmatrix} = \begin{bmatrix} d_{11} & d_{12} & d_{13} & d_{14} & d_{15} & d_{16} \\ d_{21} & d_{22} & d_{23} & d_{24} & d_{25} & d_{26} \\ d_{31} & d_{32} & d_{33} & d_{34} & d_{35} & d_{36} \end{bmatrix} \begin{bmatrix} E_x(\omega)E_x(\omega) \\ E_y(\omega)E_y(\omega) \\ E_z(\omega)E_z(\omega) \\ 2E_y(\omega)E_z(\omega) \\ 2E_x(\omega)E_z(\omega) \\ 2E_x(\omega)E_y(\omega) \end{bmatrix}$$

For the electrical field components (E_x, E_y, E_z) at the focus plane, because of the low numerical aperture of the used objective lens, E_z could be neglected. Considering an electrical field E_0 of the pump laser polarized along a direction with an angle θ to the x axis, there are expressions of $E_x = E_0 \cos(\theta)$

DOI: 10.1021/acsphotonics.8b00685
ACS Photonics 2018, 5, 3485−3491

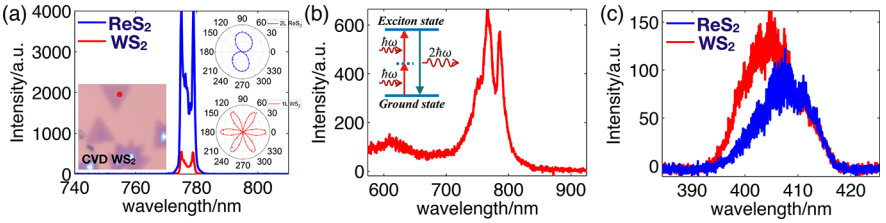

Figure 4. (a) SH spectra from the bilayer ReS_2 and the monolayer WS_2 pumped by a laser at 1558 nm. Left inset: optical microscope image of the CVD monolayer WS_2; Right inset: polar plots of SHG parallel components from the bilayer ReS_2 and monolayer WS_2. (b) Photoluminescence spectrum of the bilayer ReS_2 pumped by a laser at 532 nm. Inset indicates the two-photon resonant SHG via excitonic effects due to the consistent photon energy of the SH signal and ReS_2's exciton emission. (c) SH spectra from the bilayer ReS_2 and the monolayer WS_2 pumped by a laser at 810 nm.

and $E_y = E_0 \sin(\theta)$. The generated SH polarization components (P_x, P_y, P_z) can be regarded as electrical dipoles oscillating at the SH frequency. The SH signal radiated from P_z can not be collected by the objective lens with low numerical aperture. Therefore, only P_x and P_y contribute to the detected SH intensity. The parallel and perpendicular components of the SH intensities could be described as

$$I_{\parallel} \propto (P_x \cos(\theta) + P_y \sin(\theta))^2 = [d_{11} \cos^3(\theta) + (d_{12} + 2d_{26})\cos(\theta)\sin^2(\theta) + (d_{21} + 2d_{16})\cos^2(\theta)\sin(\theta) + d_{22} \sin^3(\theta)]^2 \quad (1)$$

$$I_{\perp} \propto (P_x \sin(\theta) - P_y \cos(\theta))^2 = [d_{12} \sin^3(\theta) + (d_{11} - 2d_{26})\cos^2(\theta)\sin(\theta) + (2d_{16} - d_{22})\cos(\theta)\sin^2(\theta) - d_{21} \cos^3(\theta)]^2 \quad (2)$$

By exploiting eqs 1 and 2 to fit the polarization dependence in Figure 2f, we could obtain the relative values of susceptibility elements of $d_{11} = 0.65$, $d_{12} = 0.6$, $d_{16} = 0.06$, $d_{21} = 0.05$, $d_{22} = 0.05$, and $d_{26} = 0.125$. Unlike 2H TMDCs, the even-layer ReS_2 belongs to the C_1 space group and the various tensor elements do not have to be equal or zero due to the low symmetry. The zero E_z and uncollected P_z unfortunately lead to the failed calculation of other elements, which could be measured with the assistance of tilted far-field microscopy[28] or near-field plasmonic modes[29,30] to extract the out-of-plane SH polarizations.

The SHG efficiency in the bilayer ReS_2 is evaluated as well. We first compare it with the SHG from a chemical vapor deposition (CVD) grown monolayer WS_2. With the same conditions of laser excitation and signal collection, as well as the same pump power, we measure SHGs from the bilayer ReS_2 and monolayer WS_2. Figure 4a plots the obtained SH spectra from the two samples when pumped by the 1558 nm pulsed laser with the same power. In the right insets, we also display the polarization-dependences of their parallel components. Anisotropic and isotropic distributions are obtained from the bilayer ReS_2 and monolayer WS_2, respectively. Note that, since the complex dispersion and nonlinear processes in the fiber laser, the output spectrum of the pump laser has multiple peaks. Correspondingly, there are multiple peaks in the SH spectra, locating between the range of 775 and 779 nm. While monolayer WS_2 is reported to have the highest second-order nonlinearity among the TMDCs,[34] the SHG from the bilayer ReS_2 is about 8× stronger than that from the monolayer WS_2. The significant SHG efficiency in the bilayer ReS_2 is originated from the resonant enhancementvia the excitonic effect. Figure 4b displays the measured photoluminescence spectrum from the bilayer ReS_2, presenting exciton emission peaks at the wavelengths of 770 and 790 nm, which agree with the results obtained in ref 17. The SH signal is on-resonant with ReS_2's exciton considering their consistent photon energy, as indicated in the inset of Figure 4b. Due to exciton's high density of state, at the corresponding transition energy, the light−matter interaction is strongly enhanced compared to the transitions in the continuum of unbound electrons and holes,[35] which therefore enables a remarkable SHG response.[22,26,34] For the monolayer WS_2 with an exciton emission around 650 nm, the off-resonance SHG has low conversion efficiency. We also pump the two samples with a femtosecond laser centered at 810 nm with a repetition rate of 80 MHz, and the obtained SH spectra are shown in Figure 4c. The two atomically thin materials present the comparable off-resonance SHG.

The above experimental results indicate the bilayer ReS_2 has a high SHG efficiency with a pump around 1558 nm due to the two-photon resonance with its exciton. We then calculate the absolute second-order sheet susceptibility at this wavelength by normalizing the SH intensity from ReS_2 (I_{ReS_2}) to the reference SH intensity from the surface of a z-cut bulk crystal of lithium niobate (I_{LN}) when pumped by the 1558 nm laser, which can be expressed as[36]

$$\chi^{(2)}_{ReS_2} = \frac{1}{16\pi\Delta k_{LN}\Delta h} \frac{[n_{LN}(\omega) + 1]^3}{n_{LN}(\omega)n_{LN}^{1/2}(2\omega)} \left(\frac{I_{ReS_2}(2\omega)}{I_{LN}(2\omega)}\right)^{1/2} \chi^{(2)}_{LN} \quad (3)$$

where $\Delta h \sim 1.6$ nm is the thickness of the bilayer ReS_2, $n_{LN}(\omega)$ and $n_{LN}(2\omega)$ are refractive indices of the light with frequencies of ω and 2ω in lithium niobate, which define their wavenumber difference Δk_{LN}, and $\chi^{(2)}_{LN}$ is lithium niobate's nonlinear susceptibility. By counting Δk_{LN} and $\chi^{(2)}_{LN}$, $\chi^{(2)}_{ReS_2}$ is estimated as 900 pm/V. Because of resonant enhancement via the excitonic effect, the bilayer ReS_2 has an effective nonlinear susceptibility that is remarkably large among the 2D materials when pumped by a telecom-band laser.

In summary, we experimentally observed unexpected layer-dependent, strong, and anisotropic SHGs in atomically thin ReS_2. Different from the well-studied group VI TMDCs, ReS_2 as the group VII TMDC has a distorted $CdCl_2$ crystal structure. While its monolayer, other odd numbers of layers and bulk crystal belong to C_i space group and have inversion symmetry, the inversion symmetries in even numbers of layers are broken. Thus, ReS_2 presents strong (negligible) SHG in even (odd) layer thickness, which is opposite to layer-dependence of SHG in group VI TMDCs. The exactly zero SHG in ReS_2 monolayer and strong SHGs in even numbers of ReS_2 layers indicate the unexpected strong interlayer coupling,

DOI: 10.1021/acsphotonics.8b00685
ACS Photonics 2018, 5, 3485−3491

which generated appreciable SH polarizations. In a bilayer ReS_2, we obtain an effective second-order nonlinear susceptibility of 900 pm/V pumped by a telecom-band laser, which is remarkably high among those reported in 2D materials. The laser polarization dependence of ReS_2's SHG is strongly anisotropic and indicates its distorted lattice structure with more unequal and nonzero second-order susceptibility elements. Our results not only reveal another distinct property between group VI and group VII TMDCs, but also open up opportunities for studying piezoelectricity and valley-dependent physics in even numbers of ReS_2 layers arising from the broken inversion symmetry.

AUTHOR INFORMATION

Corresponding Authors

*E-mail: xuetaogan@nwpu.edu.cn.
*E-mail: jlzhao@nwpu.edu.cn.

ORCID

Xuetao Gan: 0000-0003-2469-5807
Ping-Heng Tan: 0000-0001-6575-1516

Notes

The authors declare no competing financial interest.

ACKNOWLEDGMENTS

Financial support was provided by the Key Research and Development Program (2017YFA0303800, 2016YFA0301204), NSFC (61522507, 61775183, 11634010, 11474277, and 11434010), the Key Research and Development Program in Shaanxi Province of China (2017KJXX-12), and the Fundamental Research Funds for the Central Universities (3102017jc01001, 3102018jcc034). We thank Wei Ji and Jingsi Qiao for many fruitful discussions as well as the AFM measurements by the Analytical and Testing Center of NPU.

REFERENCES

(1) Mak, K. F.; He, K.; Lee, C.; Lee, G. H.; Hone, J.; Heinz, T. F.; Shan, J. Tightly Bound Trions in Monolayer MoS_2. *Nat. Mater.* **2013**, *12*, 207−211.

(2) Lee, J.; Mak, K. F.; Shan, J. Electrical Control of the Valley Hall Effect in Bilayer MoS_2 Transistors. *Nat. Nanotechnol.* **2016**, *11*, 421−425.

(3) Ross, J. S.; Rivera, P.; Schaibley, J.; Lee-Wong, E.; Yu, H.; Taniguchi, T.; Watanabe, K.; Yan, J.; Mandrus, D.; Cobden, D.; Yao, W.; Xu, X. Interlayer Exciton Optoelectronics in a 2D Heterostructure p-n Junction. *Nano Lett.* **2017**, *17*, 638−643.

(4) Wang, J.; Yao, Q.; Huang, C.; Zou, X.; Liao, L.; Chen, S.; Fan, Z.; Zhang, K.; Wu, W. W.; Xiao, X.; Jiang, C.; Wu, W. High Mobility MoS_2 Transistor with Low Schottky Barrier Contact by Using Atomic Thick h-BN as a Tunneling Layer. *Adv. Mater.* **2016**, *28*, 8302−8308.

(5) Yu, Z.; Ong, Z. Y.; Li, S.; Xu, J. B.; Zhang, G.; Zhang, Y. W.; Shi, Y.; Wang, X. Analyzing the Carrier Mobility in Transition-Metal Dichalcogenide MoS_2 Field-Effect Transistors. *Adv. Funct. Mater.* **2017**, *27*, 1604093.

(6) Wang, X.; Wang, P.; Wang, J.; Hu, W.; Zhou, X.; Guo, N.; Huang, H.; Sun, S.; Shen, H.; Lin, T.; Tang, M.; Liao, L.; Jiang, A.; Sun, J.; Meng, X.; Chen, X.; Lu, W.; Chu, J. Ultrasensitive and Broadband MoS_2 Photodetector Driven by Ferroelectrics. *Adv. Mater.* **2015**, *27*, 6575−6581.

(7) Wu, S.; Buckley, S.; Schaibley, J. R.; Feng, L.; Yan, J.; Mandrus, D.; Hatami, F.; Yao, W. M.; Vuckovic, J.; Majumdar, A.; Xu, X. Monolayer Semiconductor Nanocavity Lasers with Ultralow Thresholds. *Nature* **2015**, *520*, 69−72.

(8) Ye, Y.; Wong, Z. J.; Lu, X.; Ni, X.; Zhu, H.; Chen, X.; Wang, Y.; Zhang, X. Monolayer Excitonic Laser. *Nat. Photonics* **2015**, *9*, 733.

(9) Friemelt, K.; Luxsteiner, M. Ch.; Bucher, E. Optical Properties of The Layered Transition-Metal-Dichalcogenide ReS_2: Anisotropy in the Van Der Waals Plane. *J. Appl. Phys.* **1993**, *74*, 5266.

(10) Lin, Y.; Komsa, H.; Yeh, C. H.; Bjorkman, T.; Liang, Z. Y.; Ho, C. H.; Huang, Y. S.; Chiu, P.; Krasheninnikov, A. V.; Suenaga, K. Single-Layer ReS_2: Two-Dimensional Semiconductor with Tunable In-Plane Anisotropy. *ACS Nano* **2015**, *9*, 11249−11257.

(11) Chenet, D.; Aslan, O. B.; Huang, P. Y.; Fan, C.; Der Zande, A. M.; Heinz, T. F.; Hone, J. In-Plane Anisotropy in Mono- and Few-Layer ReS_2 Probed by Raman Spectroscopy and Scanning Transmission Electron Microscopy. *Nano Lett.* **2015**, *15*, 5667−5672.

(12) Lorchat, E.; Froehlicher, G.; Berciaud, S. Splitting of Interlayer Shear Modes and Photon Energy Dependent Anisotropic Raman Response in N-Layer $ReSe_2$ and $ReS2_2$. *ACS Nano* **2016**, *10*, 2752−2760.

(13) Liu, E.; Fu, Y.; Wang, Y.; Feng, Y.; Liu, H.; Wan, X.; Zhou, W.; Wang, B.; Shao, L.; Ho, C.; Huang, Y.; Cao, Z.; Wang, L.; Li, A.; Zeng, J.; Song, F.; Wang, X.; Shi, Y.; Yuan, H.; Hwang, H. Y.; Cui, Y.; Miao, F.; Xing, D. Y. Integrated Digital Inverters Based on Two-dimensional Anisotropic ReS_2 Field-effect Transistors. *Nat. Commun.* **2015**, *6*, 6991−6991.

(14) Cui, Q.; He, J.; Bellus, M. Z.; Mirzokarimov, M.; Hofmann, T.; Chiu, H.; Antonik, M.; He, D.; Wang, Y.; Zhao, H. Transient Absorption Measurements on Anisotropic Monolayer ReS_2. *Small* **2015**, *11*, 5565−5571.

(15) Wolverson, D.; Crampin, S.; Kazemi, A. S.; Ilie, A.; Bending, S. J. Raman Spectra of Monolayer, Few-Layer, and Bulk $ReSe_2$: An Anisotropic Layered Semiconductor. *ACS Nano* **2014**, *8*, 11154−11164.

(16) Qiao, X.; Wu, J.; Zhou, L.; Qiao, J.; Shi, W.; Chen, T.; Zhang, J.; Ji, W.; Tan, P. Polytypism and Unexpected Strong Interlayer Coupling of two-Dimensional Layered ReS_2. *Nanoscale* **2016**, *8*, 8324−8332.

(17) Aslan, O. B.; Chenet, D.; Der Zande, A. M.; Hone, J.; Heinz, T. F. Linearly Polarized Excitons in Single- and Few-Layer ReS_2 Crystals. *ACS Photonics* **2016**, *3*, 96−101.

(18) Arora, A.; Noky, J.; DrŸppel, M.; Jariwala, B.; Deilmann, T.; Schneider, R.; Schmidt, R.; Pozo-Zamudio, O. D.; Stiehm, T.; Bhattacharya, A.; Krger, P.; Vasconcellos, S. M. D.; Rohlfing, M.; Bratschitsch, R. Highly Anisotropic in-Plane Excitons in Atomically Thin and Bulklike 1 T′-$ReSe_2$. *Nano Lett.* **2017**, *17*, 3202−3207.

(19) Zhang, E.; Wang, P.; Li, Z.; Wang, H.; Song, C.; Huang, C.; Chen, Z.; Yang, L.; Zhang, K.; Lu, S.; Wang, W.; Liu, S.; Fang, H.; Zhou, X.; Yan, H.; Zou, J.; Wan, X.; Zhou, P.; Hu, W.; Xiu, F. Tunable Ambipolar Polarization-Sensitive Photodetectors Based on High-Anisotropy $ReSe_2$ Nanosheets. *ACS Nano* **2016**, *10*, 8067−8077.

(20) Tongay, S.; Sahin, H.; Ko, C.; Luce, A.; Fan, W.; Liu, K.; Zhou, J.; Huang, Y. S.; Ho, C. H.; Yan, J.; Ogletree, D. F.; Aloni, S.; Ji, J.; Li, S.; Li, J.; Peeters, F. M.; Wu, J. Monolayer Behavior in Bulk ReS_2 Due to Electronic and Vibrational Decoupling. *Nat. Commun.* **2014**, *5*, 1−6.

(21) Zhang, E.; Jin, Y.; Yuan, X.; Wang, W.; Zhang, C.; Tang, L.; Liu, S.; Zhou, P.; Hu, W.; Xiu, F. ReS_2-Based Field-Effect Transistors and Photodetectors. *Adv. Funct. Mater.* **2015**, *25*, 4076−4082.

(22) Malard, L. M.; Alencar, T. V.; Barboza, A. P. M.; Mak, K. F.; Paula, A. M. D. Observation of Intense Second Harmonic Generation from MoS_2 Atomic Crystals. *Phys. Rev. B: Condens. Matter Mater. Phys.* **2013**, *87*, na.

(23) Li, Y.; Rao, Y.; Mak, K. F.; You, Y.; Wang, S.; Dean, C. R.; Heinz, T. F. Probing Symmetry Properties of Few-Layer MoS_2 and h-BN by Optical Second-Harmonic Generation. *Nano Lett.* **2013**, *13*, 3329.

(24) Tan, P. H.; Han, W. P.; Zhao, W. J.; Wu, Z. H.; Chang, K.; Wang, H.; Wang, Y. F.; Bonini, N.; Marzari, N.; Pugno, N.; Savini, G.; Lombardo, A.; Ferrari, A. C. The Shear Mode of Multilayer Graphene. *Nat. Mater.* **2012**, *11*, 294.

DOI: 10.1021/acsphotonics.8b00685
ACS Photonics 2018, 5, 3485−3491

(25) Liang, L.; Zhang, J.; Sumpter, B. G.; Tan, Q. H.; Tan, P. H.; Meunier, V. Low-Frequency Shear and Layer-Breathing Modes in Raman Scattering of Two-Dimensional Materials. *ACS Nano* **2017**, *11*, 11777.
(26) Le, C. T.; Clark, D. J.; Ullah, F.; Senthilkumar, V.; Jang, J. I.; Sim, Y.; Seong, M.-J.; Chung, K.-H.; Park, H.; Kim, Y. S. Nonlinear Optical Characteristics of Monolayer $MoSe_2$. *Ann. Phys.* **2016**, *528* (7−8), 551−559.
(27) Zhang, S.; Dong, N.; McEvoy, N.; O'Brien, M.; Winters, S.; Berner, N. C.; Yim, C.; Li, Y.; Zhang, X.; Chen, Z.; Zhang, L.; Duesberg, G. S.; Wang, J. Direct Observation of Degenerate Two-Photon Absorption and Its Saturation in WS_2 and MoS_2 Monolayer and Few-Layer Films. *ACS Nano* **2015**, *9* (7), 7142−7150.
(28) Lu, A. Y.; Zhu, H.; Xiao, J.; Chuu, C. P.; Han, Y.; Chiu, M. H.; Cheng, C. C.; Yang, C. W.; Wei, K. H.; Yang, Y.; Wang, Y.; Sokaras, D.; Nordlund, D.; Yang, P.; Muller, D.; Chou, M. Y.; Zhang, X.; Li, L. J. Janus Monolayers of Transition Metal Dichalcogenides. *Nat. Nanotechnol.* **2017**, *12*, 744−749.
(29) Park, K. D.; Jiang, T.; Clark, G.; Xu, X.; Raschke, M. B. Radiative Control of Dark Excitons at Room Temperature by Nano-Optical Antenna-Tip Purcell Effect. *Nat. Nanotechnol.* **2018**, *13*, 59−64.
(30) Zhou, Y.; Scuri, G.; Wild, D. S.; High, A. A.; Dibos, A.; Jauregui, L. A.; Shu, C.; Greve, K. D.; Pistunova, K.; Joe, A. Y.; Taniguchi, T.; Watanabe, K.; Kim, P.; Lukin, M. D.; Park, H. Probing Dark Excitons in Atomically Thin Semiconductors via Near-Field Coupling to Surfaceplasmon polaritons. *Nat. Nanotechnol.* **2017**, *12*, 856−860.
(31) Kravtsov, V.; AlMutairi, S.; Ulbricht, R.; Kutayiah, A. R.; Belyanin, A.; Raschke, M. B. Enhanced Third-Order Optical Nonlinearity Driven by Surface-Plasmon Field Gradients. *Phys. Rev. Lett.* **2018**, *120* (20), 203903.
(32) Shen, Y. R. *The Principles of Nonlinear Optics*; Wiley-Interscience: New York, 2003.
(33) Boyd, R. W. *Nonlinear Opt.*, 3rd ed.; Academy Press: San Diego, CA, 2008.
(34) Janisch, C.; Wang, Y.; Ma, D.; Mehta, N.; Elias, A. L.; Perealopez, N.; Terrones, M.; Crespi, V. H.; Liu, Z. Extraordinary Second Harmonic Generation in Tungsten Disulfide Monolayers. *Sci. Rep.* **2015**, *4*, 5530.
(35) Wang, G.; Chernikov, A.; Glazov, M. M.; Heinz, T. F.; Marie, X.; Amand, T.; Urbaszek, B. Colloquium: Excitons in Atomically Thin Transition Metal Dichalcogenides. *Rev. Mod. Phys.* **2018**, *90*, 021001.
(36) Clark, D. J.; Senthilkumar, V.; Le, C. T.; Weerawarne, D. L.; Shim, B.; Jang, J. I.; Shim, J. H.; Cho, J.; Sim, Y.; Seong, M. J.; Rhim, S. H.; Freeman, A. J.; Chung, K. H.; Kim, Y. S. Strong Optical Nonlinearity of CVD-Grown MoS_2 Monolayer as Probed by Wavelength-Dependent Second-Harmonic Generation. *Phys. Rev. B: Condens. Matter Mater. Phys.* **2014**, *90*, 121409.

DOI: 10.1021/acsphotonics.8b00685
ACS Photonics 2018, 5, 3485−3491